

Article

# Electrocatalytic Performance of Carbon Supported WO<sub>3</sub>-Containing Pd–W Nanoalloys for Oxygen Reduction Reaction in Alkaline Media

Nan Cui, Wenpeng Li \*, Zengfeng Guo, Xun Xu and Hongxia Zhao

Key Lab of Fine Chemicals in Universities of Shandong, Institute of Advanced Energy Materials and Chemistry, School of Chemistry and Pharmaceutical Engineering, Qilu University of Technology (Shandong Academy of Sciences), Daxue Road, Changqing District, Jinan 250353, China; cuinan0565@163.com (N.C.); gzf201605@163.com (Z.G.); xun0121@outlook.com (X.X.); hongxiashao@sina.com (H.Z.)

\* Correspondence: liwenpeng@qlu.edu.cn or wenpengli75@163.com; Tel.: +86-531-8963-1208

Received: 7 April 2018; Accepted: 21 May 2018; Published: 24 May 2018



**Abstract:** In this paper, we report that WO<sub>x</sub> containing nanoalloys exhibit stable electrocatalytic performance in alkaline media, though bulk WO<sub>3</sub> is easy to dissolve in NaOH solution. Carbon supported oxide-rich Pd–W alloy nanoparticles (PdW/C) with different Pd:W atom ratios were prepared by the reduction–oxidation method. Among the catalysts, the oxide-rich Pd<sub>0.8</sub>W<sub>0.2</sub>/C (Pd/W = 8:2, atom ratio) exhibits the highest catalytic activity for the oxygen reduction reaction. The X-ray photoelectron spectroscopy data shows that ~40% of Pd atoms and ~60% of the W atoms are in their oxide form. The Pd 3d<sub>5/2</sub> binding energy of the oxide-rich Pd–W nanoalloys is higher than that of Pd/C, indicating the electronic structure of Pd is affected by the strong interaction between Pd and W/WO<sub>3</sub>. Compare to Pd/C, the onset potential of the oxygen reduction reaction at the oxide-rich Pd<sub>0.8</sub>W<sub>0.2</sub>/C shifts to a higher potential. The current density (mA·mg Pd<sup>−1</sup>) at the oxide-rich Pd<sub>0.8</sub>W<sub>0.2</sub>/C is ~1.6 times of that at Pd/C. The oxide-rich Pd<sub>0.8</sub>W<sub>0.2</sub>/C also exhibits higher catalytic stability than Pd/C, which demonstrates that it is a prospective candidate for the cathode of fuel cells operating with alkaline electrolyte.

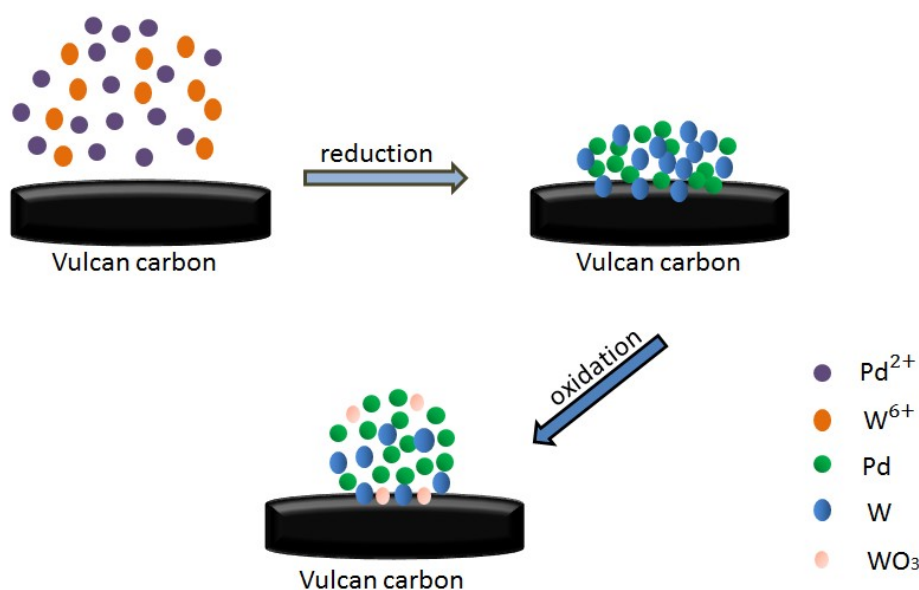
**Keywords:** WO<sub>3</sub>; electrocatalysts; alkaline; Pd–W alloy; oxygen reduction reaction; reduction–oxidation method

## 1. Introduction

The study of the oxygen reduction reaction (ORR) has a history of more than one century since Grove fabricated the earliest hydrogen–oxygen fuel cell with Pt as the catalyst for ORR in 1839. In recent years, the studies of ORR have been promoted by the increasing demand of clean energy technology like fuel cells. As the energy efficiency and battery voltage of electrochemical cells are limited by the slow kinetics of the ORR [1,2], there is a great need for highly efficient catalysts for ORR. Various electrocatalysts for ORR have been developed, including but not limited to Pt-based catalysts [3–5], Pd-based catalysts [6,7], catalysts based on non-precious metals [8,9], catalysts based on carbon nanostructure/nanocomposites [10–13], catalysts based on metal oxides [14,15], catalysts based on metal–organic frameworks [16,17], catalysts based on complexes [18,19], enzyme-based catalysts [20–24], metal carbides [25–28], and so on. Among the catalysts for ORR, Pt-based catalysts are regarded as the most active catalysts [29]. However, platinum's scarcity limits the large scale application of Pt-based electrocatalysts. Palladium has been used as one of the alternative candidates being about 200 times more abundant in the earth than platinum. There have been some reviews about Pd-based electrocatalysts [30–32]. The ORR [33] can be performed under both acid conditions and alkaline conditions in fuel cells. It has been reported that alkaline media are a benefit for the kinetics

of ORR [34]. In alkaline solutions, the oxygen can be reduced through a four-electron pathway or a two-electron pathway [35]. A lot of novel Pd-based electrocatalysts for ORR exist, including carbon or metal supported Pd alloys [36–38], nitrogen and sulfur co-doped carbon supported PdNi catalyst (PdNi-NS/C) [39], Pd supported on TiO<sub>2</sub> with oxygen vacancy (Pd/TiO<sub>2</sub>-Vo) [40], PdW nanoparticles supported on sulfur-doped graphene (PdW/SG) [41], PdNiCu/PdNiCo supported on nitrogen doped graphene [42], PdSnCo/nitrogen-doped-graphene [43], electrochemically reduced graphene-oxide supported Pd-Mn<sub>2</sub>O<sub>3</sub> nanoparticles [44], AuPd@PdAu alloy nanocrystals [45], three-dimensional nitrogen-doped graphene supports for palladium nanoparticles (Pd-N/3D-GNS) [46], and so on. Most of the research above on Pd-based electrocatalysts for ORR in alkaline media is supported on graphene specially treated (doping, modifying, and so on). Although carbon black is the most used support for noble metal electrocatalysts in fuel cells, Pd-based electrocatalysts supported on carbon black (C) for ORR in alkaline media have been rarely reported over the past few years. Besides the boom of novel support materials like doped graphene, one of the possible reasons is the high activity of Pd/C for ORR in alkaline media. It was found that Pd/C exhibits significantly high activity close to Pt/C in alkaline solutions [37,38], therefore it is difficult for other electrocatalysts for ORR in alkaline media to exhibit much higher activity than Pd/C. The new studies about carbon-black supporting Pd based catalysts for ORR in alkaline media have to face the difficult situation of being compared to the ultra-high active catalyst Pd/C.

After their calculations based on quantum mechanics, Goddard et.al. [47] predicted that Pd<sub>3</sub>W was a prospective catalyst for ORR, which was confirmed by our previous work for Pd<sub>0.7</sub>W<sub>0.3</sub> in acid media [48]. To date, Pt-based electrocatalysts are commonly used in commercially available electric vehicles powered by fuel cells. Goddard and his coworkers examined the critical barriers of the ORR with Pd<sub>3</sub>W and compared them to the analogous barriers for Pd and Pt. The results demonstrated that Pd<sub>3</sub>W exhibits ORR properties greatly improved over pure Pd and close to that of pure Pt. Since the cost of Pd<sub>3</sub>W is six times less than that of pure Pt, a highly efficient Pd–W system is a promising candidate for future application. In this work, we attempt to fabricate high performance Pd–W/C systems for ORR in alkaline media. Most of the noble metal electrocatalysts used in fuel cells are in the form of nanoparticles supported on carbon. Since the surface of metal nanoparticles is easy to be oxidized by ambient air, the effect of oxides in the Pd-based catalysts for ORR in alkaline media should be discussed. There have been some state-of-art electrocatalysts based on oxides such as Fe<sub>3</sub>O<sub>4</sub>@NiFexO<sub>y</sub> [49]. However, as the resistance of semiconductor oxides is higher than that of metals, the output voltage will decrease when the oxides are directly used as electrode materials in fuel cells or metal–air batteries. Combining the oxide with a high-conductive metal in each of the nanoparticles of catalysts is a solution for avoiding the decrease. The interaction of metal and metal oxides in catalysts has attracted research interests for decades [50–53]. It has been reported recently that metal and metal oxides interactions are greatly affected by the catalytic consequence of electrocatalysis reactions such as the oxygen reduction reaction [54] and the ethanol oxidation reaction [55,56]. Bulk WO<sub>3</sub> crystal can be dissolved in strong NaOH solutions, which limits its direct application in fuel cells operating with alkaline electrolytes. To solve this problem, we started by separating the W atoms with noble metals such as Pd in the atomic scale before their oxidation. Therefore the chemical bonds attached to most of the W atoms are not W–O–W bonds but Pd–W metallic bonds, which are more stable than W–O–W bonds in alkaline solutions. According to the Monte Carlo simulation [57,58], alloy clusters at the surface of nano-materials sometimes exhibit higher stability. Then, we fabricated WO<sub>x</sub>-containing Pd–W nanoalloys with the reduction–oxidation method (Scheme 1). The onset potential of ORR at the as prepared oxide-rich Pd<sub>0.8</sub>W<sub>0.2</sub>/C (Pd/W = 8:2, metal atomic ratio) is close to the Pd/C and Pt/C fabricated with the chemical reduction method [36]. The ORR stability and current density (mA·mg Pd<sup>-1</sup>) of the oxide-rich Pd<sub>0.8</sub>W<sub>0.2</sub>/C are higher than those of Pd/C, which indicates that the oxide-rich Pd<sub>0.8</sub>W<sub>0.2</sub>/C is a prospective candidate for the cathode of fuel cells.



**Scheme 1.** Schematic illustration of the formation of catalyst. Dimensions are not to scale.

## 2. Results and Discussion

### 2.1. Characterization of Oxide-Rich PdW/C Catalysts

The X-ray diffraction (XRD) patterns of Pd/C (a), oxide-rich Pd<sub>0.6</sub>W<sub>0.4</sub>/C (b), Pd<sub>0.7</sub>W<sub>0.3</sub>/C (c), Pd<sub>0.8</sub>W<sub>0.2</sub>/C (d), Pd<sub>0.9</sub>W<sub>0.1</sub>/C (e) are shown in Figure 1. Five typical diffraction peaks of the catalysts are observed at about 24.8°, 40°, 46°, 68°, 82° in the diffractogram. The five peaks correspond to the Vulcan XC-72R carbon (002) crystal face, face centered cubic (fcc) metal Pd (111), (200), (220) and (311) crystal plane diffraction, respectively. The XRD patterns do not show any diffraction peaks corresponding to W (fcc) or WO<sub>3</sub> indicating that most of the W atoms do not exist as an individual phase, but have entered into the lattice of the Pd crystal. The absence of peaks for tungsten also was found in our previous reported Pd<sub>0.7</sub>W<sub>0.3</sub> catalyst [59] used in acid conditions. The diffraction angle of (220) or (311) crystal plane diffraction peaks of the Pd in the PdW/C catalysts is higher than that of the corresponding Pd/C catalyst. The XRD peaks shift to a higher angle indicating compression in the direction perpendicular to the tensile stress [60,61]. The size of catalyst metal particles can be estimated with Scherrer's equation [62]. The estimated particle size of Pd/C, Pd<sub>0.6</sub>W<sub>0.4</sub>/C, Pd<sub>0.7</sub>W<sub>0.3</sub>/C, Pd<sub>0.8</sub>W<sub>0.2</sub>/C and Pd<sub>0.9</sub>W<sub>0.1</sub>/C were 5.6 nm, 4.8 nm, 4.5 nm, 4.3 nm, and 5.2 nm, respectively. The particle size of the oxide-rich Pd–W/C nanoparticles is smaller than that of Pd/C.

The morphology and particle distribution (Figure 2) of Pd/C (a, b) and oxide-rich Pd<sub>0.8</sub>W<sub>0.2</sub>/C (c, d) were characterized by transmission electron microscope (TEM). The oxide-rich Pd<sub>0.8</sub>W<sub>0.2</sub> nanoparticles are more uniformly dispersed on the carbon surface than Pd. The average diameter of Pd nanoparticles is 5.6 nm while the average metal particle diameter of oxide-rich Pd<sub>0.8</sub>W<sub>0.2</sub> is 4.3 nm which are consistent with the XRD results. Figure 3a–c shows high resolution transmission electron microscopy (HRTEM) of oxide-rich Pd<sub>0.8</sub>W<sub>0.2</sub>/C catalyst. The lattice spacing in Figure 3a–c is 0.224 nm, 0.193 nm and 0.263 nm which respectively correspond to the (111), (200) crystal planes of face-centered cubic Pd and (220) plane of WO<sub>3</sub>. The lattice fringes of WO<sub>3</sub> can be found in a few nanoparticles, which supports the existence of WO<sub>x</sub> in the Pd<sub>0.8</sub>W<sub>0.2</sub>/C catalysts. Although the WO<sub>3</sub> phase is found in a few nanoparticles, there is no W phase or WO<sub>3</sub> phase in most of the Pd–W alloy nanoparticles, which is consistent with the XRD patterns. It indicates that most of the W atoms have been mixed with the Pd atoms during the preparation of Pd–W alloy nanoparticles from the uniform mixtures of Pd salt and W salt, thus the separate W or WO<sub>3</sub> phase is rare. Besides, the W atoms on the surface of Pd–W nanoparticles are easily oxidized by ambient air, therefore it is difficult to find the W phase on

the surface of Pd–W nanoparticles. Although there is no diffraction peak corresponding to W in the XRD patterns mentioned above, the energy dispersive spectrum (EDS) of the as prepared oxide-rich Pd<sub>0.8</sub>W<sub>0.2</sub>/C (Figure 3d) shows the content of W in the Pd–W nanoalloys.

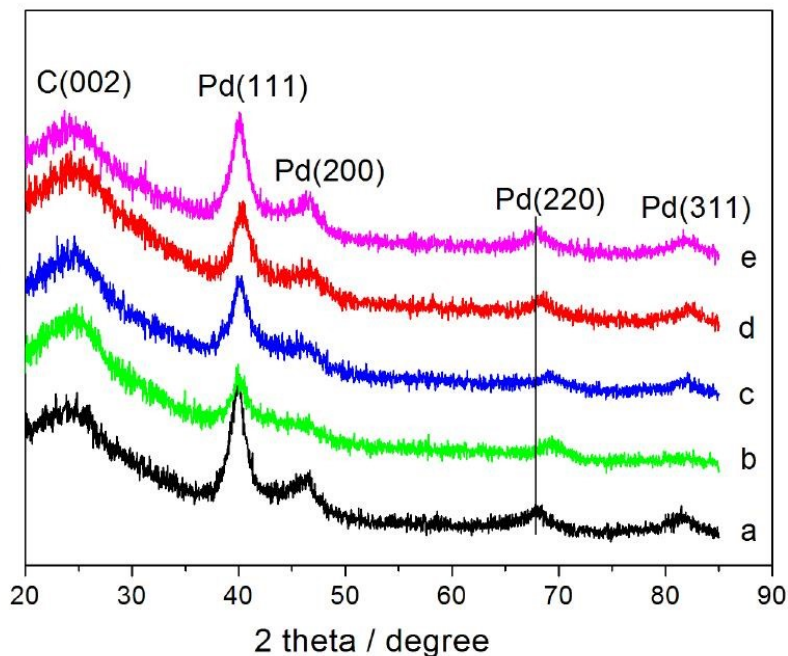


**Figure 1.** X-ray diffraction (XRD) patterns of Pd/C (a), oxide-rich Pd<sub>0.6</sub>W<sub>0.4</sub>/C (b), oxide-rich Pd<sub>0.7</sub>W<sub>0.3</sub>/C (c), oxide rich Pd<sub>0.8</sub>W<sub>0.2</sub>/C (d), and oxide rich Pd<sub>0.9</sub>W<sub>0.1</sub>/C (e).

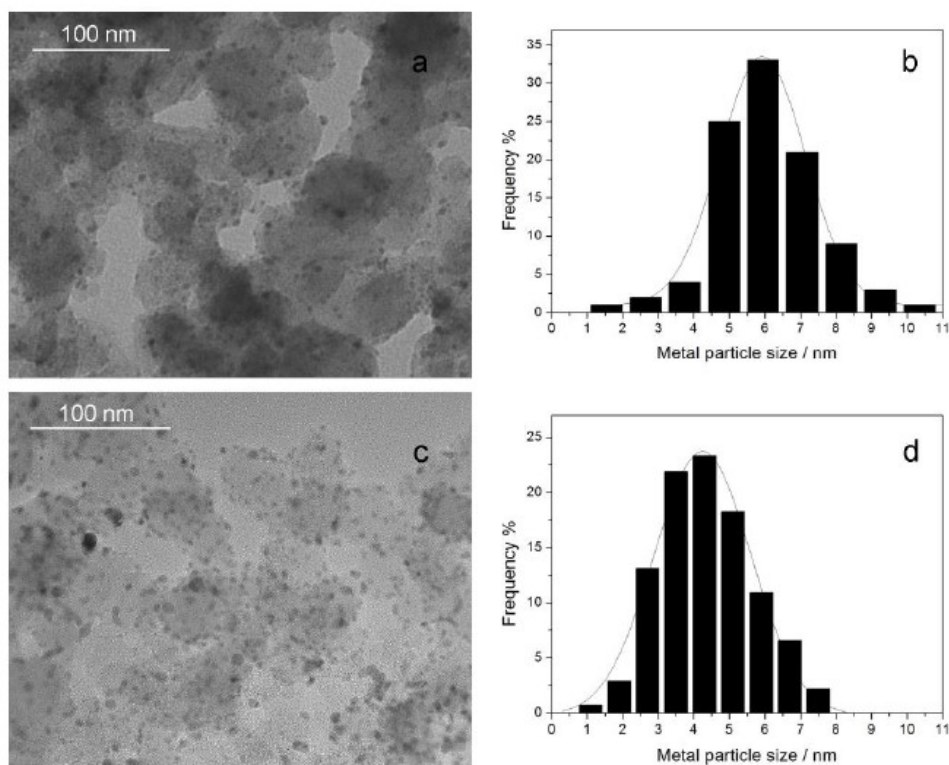


**Figure 2.** The morphology and particle distribution of Pd/C (a,b) and oxide-rich Pd<sub>0.8</sub>W<sub>0.2</sub>/C (c,d).

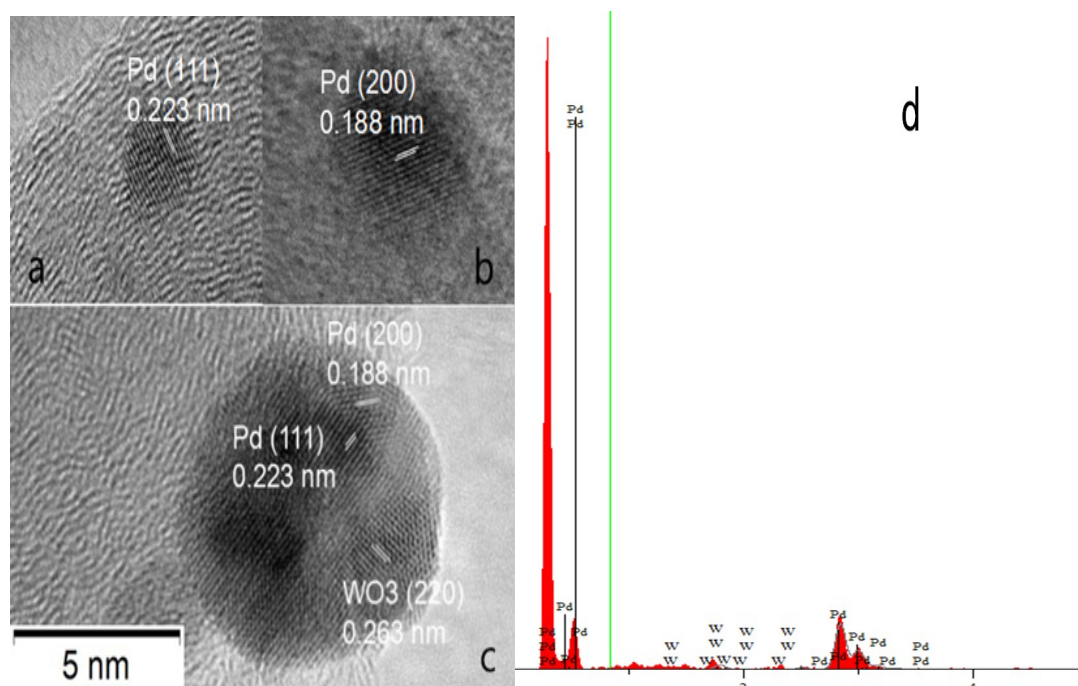


**Figure 3.** High resolution transmission electron microscopy (HRTEM) (a–c) images and energy dispersive spectroscopy (EDS) spectra (d) of the oxide-rich Pd<sub>0.8</sub>W<sub>0.2</sub>/C catalyst.

Figure 4 shows the X-ray photoelectron spectroscopy (XPS) spectra of oxide-rich Pd<sub>0.6</sub>W<sub>0.4</sub>/C, Pd<sub>0.7</sub>W<sub>0.3</sub>/C, Pd<sub>0.8</sub>W<sub>0.2</sub>/C, Pd<sub>0.9</sub>W<sub>0.1</sub>/C. The XPS spectra of Pd/C was published in our recent works [63]. All XPS curves were fitted using the Gaussian–Lorentzian (20%) method after subtracting the background with Shirley’s method. The surface composition ratios of the Pd:W elements in oxide-rich Pd<sub>0.6</sub>W<sub>0.4</sub>/C, Pd<sub>0.7</sub>W<sub>0.3</sub>/C, Pd<sub>0.8</sub>W<sub>0.2</sub>/C and Pd<sub>0.9</sub>W<sub>0.1</sub>/C are Pd<sub>0.57</sub>W<sub>0.43</sub>, Pd<sub>0.70</sub>W<sub>0.30</sub>, Pd<sub>0.79</sub>W<sub>0.21</sub>, Pd<sub>0.87</sub>W<sub>0.23</sub>, respectively. In Figure 4a, the peaks of Pd 3d<sub>5/2</sub> and Pd 3d<sub>3/2</sub> correspond to Pd and PdO<sub>y</sub> (0 < 2 < y), and the Pd element is present in all the samples as Pd metal and PdO<sub>y</sub>. The binding energy of Pd 3d<sub>5/2</sub> peaks of PdW/C catalysts respectively shifted +0.21 eV, +0.28 eV, +0.36 eV, +0.52 eV compared with that of Pd/C (335.6 eV, the solid line) which indicates a decrease of Pd 3d electronic cloud densities. The change of the electronic structure is due to the formation of high-valency oxides. Figure 4b is the peak of W<sub>4f</sub>. The two peaks at 35.5 and 37.5 eV correspond to WO<sub>3</sub>. With the decrease of tungsten content in the Pd–W nanoalloy, the atom ratio of W(0):W(VI) increases. The W(0):W(VI) in Pd<sub>0.9</sub>W<sub>0.1</sub>/C, Pd<sub>0.8</sub>W<sub>0.2</sub>/C, Pd<sub>0.7</sub>W<sub>0.3</sub>/C and Pd<sub>0.8</sub>W<sub>0.2</sub>/C is W(0)<sub>0.40</sub>:W(VI)<sub>0.60</sub>, W(0)<sub>0.42</sub>:W(VI)<sub>0.58</sub>, W(0)<sub>0.48</sub>:W(VI)<sub>0.52</sub>, W(0)<sub>0.55</sub>:W(VI)<sub>0.45</sub>, respectively. The oxides play a key role in the oxide-rich Pd–W/C electrocatalysts. It was found that the PdO exhibits higher electrocatalytic activity and stability for ORR than Pd in alkaline solutions [64]. WO<sub>3</sub> nanoarray supported on carbon cloth has been regarded as a state-of-art catalyst for the oxygen evolution reaction (OER) [65] operating in alkaline media. Zhang et al. [66] reported that Pd supported on WO<sub>3</sub>/C exhibits a higher ORR activity in acid solution than Pd/C. The strong interaction between Pd and WO<sub>3</sub> effectively promotes the direct 4-electron pathway of the ORR at Pd. In this work, the performance of the as prepared oxide-rich Pd–W/C catalyst is enhanced by both the high ORR activity of PdO and the synergistic effect of W/WO<sub>3</sub>.

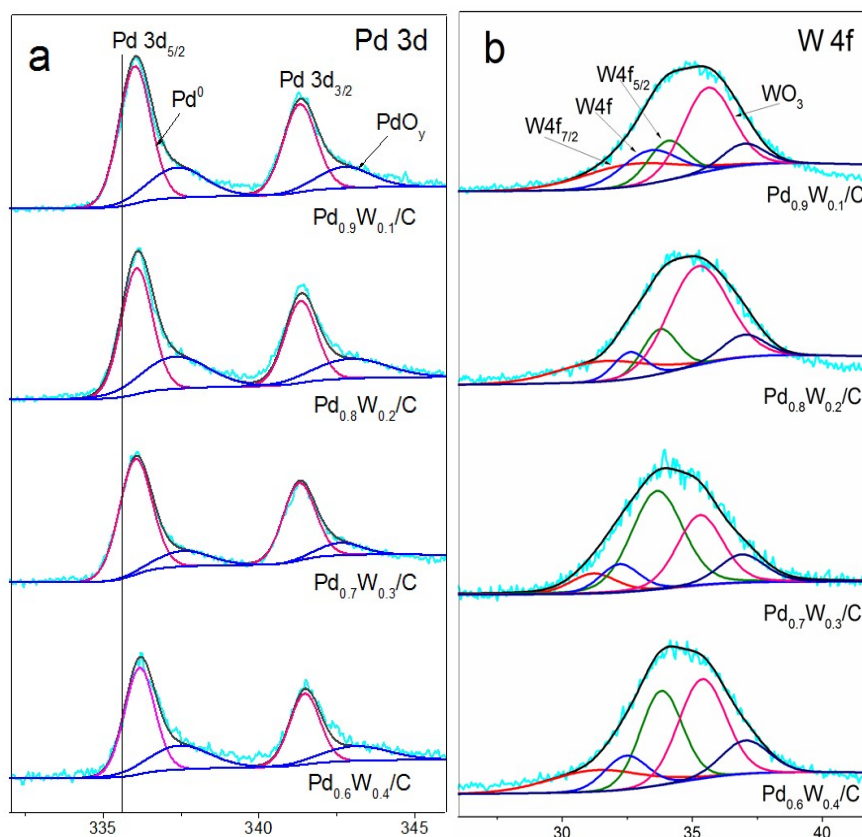


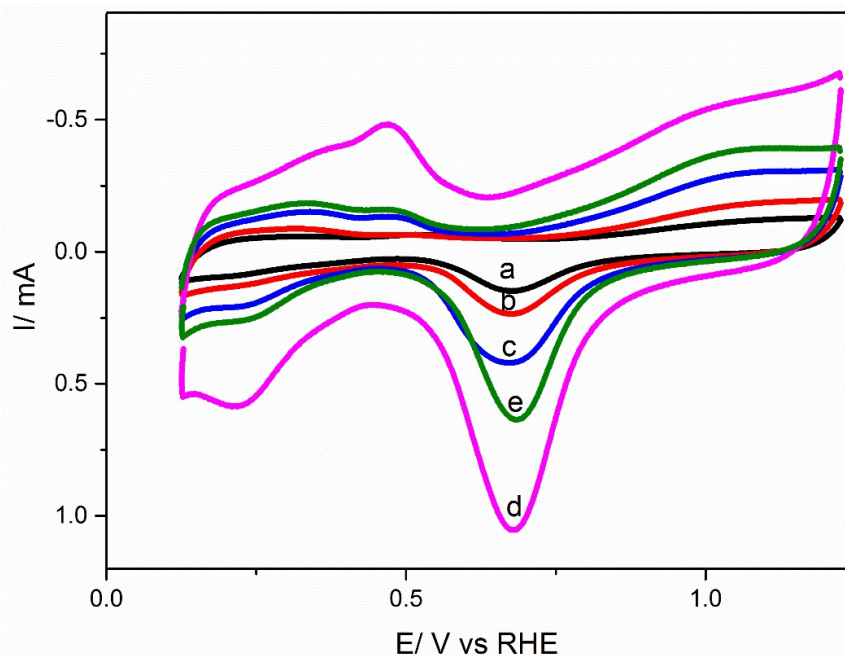
**Figure 4.** X-ray photoelectron spectroscopy (XPS) spectra of (a) Pd 3d and (b) W 4f of oxide-rich PdW/C catalysts.

## 2.2. Electrochemical Performance

Figure 5 shows the cyclic voltammograms (CV) of Pd/C (a), oxide-rich Pd<sub>0.6</sub>W<sub>0.4</sub>/C (b), Pd<sub>0.7</sub>W<sub>0.3</sub>/C (c), Pd<sub>0.8</sub>W<sub>0.2</sub>/C (d), Pd<sub>0.9</sub>W<sub>0.1</sub>/C (e); all the CVs were measured in 1 M NaOH solution at a scan rate of 10 mV·s<sup>-1</sup>. All the potentials in this paper are quoted with respect to reversible hydrogen electrode (RHE). All potentials vs. the Hg/HgO electrode were converted to values referring to the RHE using the following equation:  $E(\text{RHE}) = E(\text{Hg}/\text{HgO}) + 0.098 \text{ V} + 0.0591 \times \text{pH}$ . The peak of hydrogen adsorption/desorption is at about 0.23 V. The peak of OH<sup>-</sup> adsorbed on the surface of the electrocatalyst is in the range from 0.33 V to 0.53 V. The oxidation of the surface metal and the resulting reduction of the oxide are in the range of 0.33 V to 1.13 V. The peak at ~-0.7 V vs. RHE changed dramatically depending on the ratio of Pd and W. There are several factors affecting the current. As mentioned above, the size/diameter of the nanoparticles changed with the content of W. In a smaller nanoparticle, more metal atoms locate at the surface, which is a benefit for the electrochemical reaction. Besides, the peak at ~-0.7 V vs. RHE corresponds to the reduction of PdO at the surface of Pd–W bimetallic nanoparticles. The surface Pd content in the oxide-rich Pd–W nanoalloys changes with the Pd:W ratios. Furthermore, the peak current could also be affected by other known/unknown physical properties of the bimetallic nanoparticles. For example, as mentioned above, the addition of W changed the electron structure of Pd atoms. The electrochemical active surface area (EASA) can be calculated by the amount of charge corresponding to the hydrogen adsorption/desorption region in the cyclic voltammetric characteristic curve. However, Pd based catalysts supported on carbon have poor clarity for hydrogen because hydrogen can penetrate into the Pd-based alloy structure. So the reduction charge of PdO was chosen to calculate the EASA. The EASA value of the catalyst was calculated by the following equation:

$$\text{EASA} = Q/\text{QMR}$$

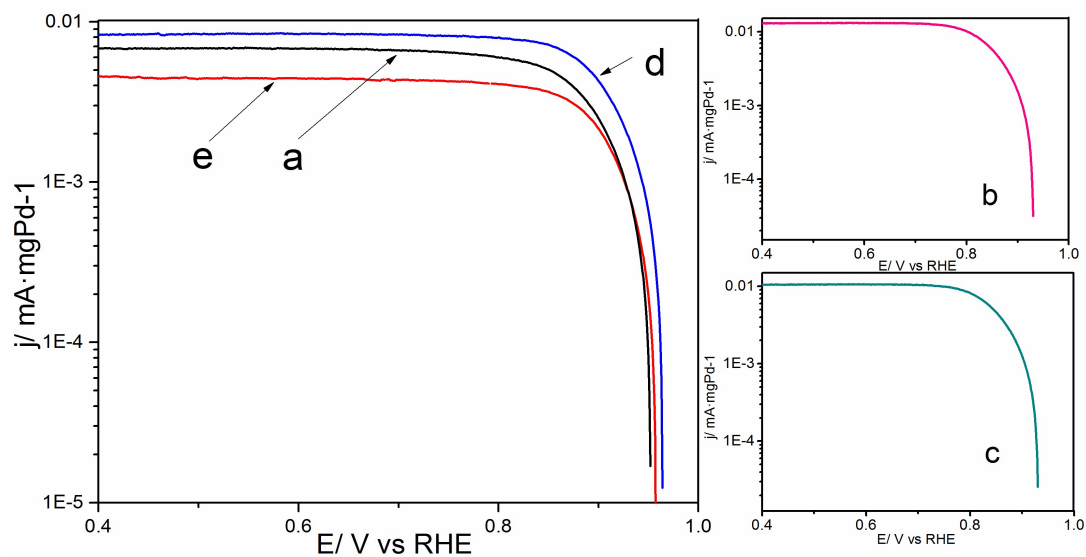
where  $Q$  is the coulombs of the reduction of palladium oxide over a range of 0.47 V to 0.87 V, and  $Q_{MR}$  is the charge required to reduce a monolayer of PdO. The single-layer palladium oxide reduction charge was  $4.05 \text{ C/m}^2$ . The EASA of Pd/C (a), oxide-rich Pd<sub>0.6</sub>W<sub>0.4</sub>/C (b), oxide-rich Pd<sub>0.7</sub>W<sub>0.3</sub>/C (c), oxide-rich Pd<sub>0.8</sub>W<sub>0.2</sub>/C (e) and oxide-rich Pd<sub>0.9</sub>W<sub>0.1</sub>/C (d) were  $7.85 \text{ cm}^2$ ,  $8.75 \text{ cm}^2$ ,  $9.91 \text{ cm}^2$ ,  $11.8 \text{ cm}^2$ , and  $19.9 \text{ cm}^2$  respectively.



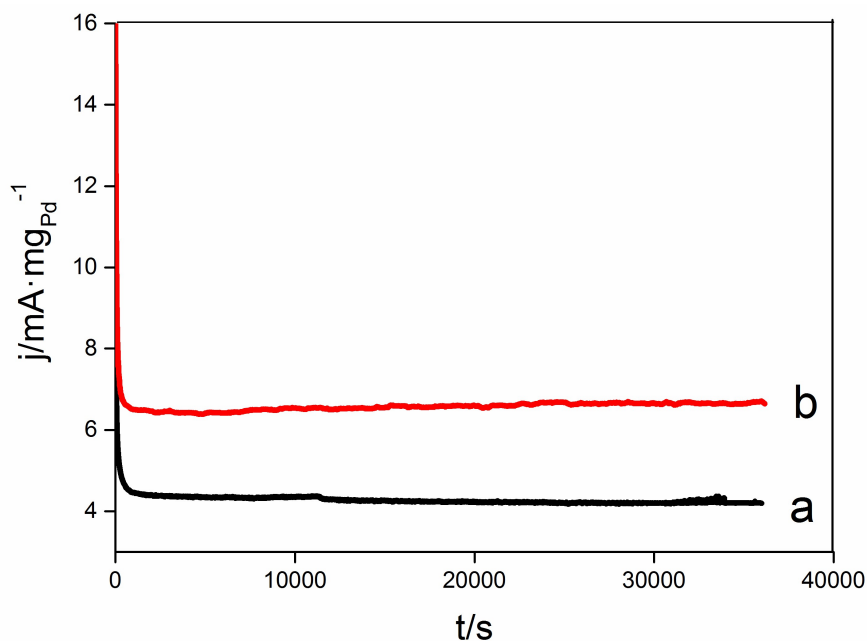
**Figure 5.** Cyclic voltammograms (CV) of Pd/C (a), oxide-rich Pd<sub>0.6</sub>W<sub>0.4</sub>/C (b), oxide-rich Pd<sub>0.7</sub>W<sub>0.3</sub>/C (c), oxide-rich Pd<sub>0.8</sub>W<sub>0.2</sub>/C (d), oxide-rich Pd<sub>0.9</sub>W<sub>0.1</sub>/C (e) in 1 M NaOH solution. Scan rate  $10 \text{ mV}\cdot\text{s}^{-1}$ .

Figure 6 displays the linear sweep voltammetry (LSV) of Pd/C (a), oxide-rich Pd<sub>0.6</sub>W<sub>0.4</sub>/C (b), Pd<sub>0.7</sub>W<sub>0.3</sub>/C (c), Pd<sub>0.8</sub>W<sub>0.2</sub>/C (d), Pd<sub>0.9</sub>W<sub>0.1</sub>/C (e) catalysts. The LSV curves were measured at a rotating disk electrode (RDE) with a rotating speed of 2000 r/min and a scan rate of  $1 \text{ mV}\cdot\text{s}^{-1}$ . The electrolyte is 0.1 M NaOH solution saturated with O<sub>2</sub>. Compared with Pd/C, the onset potential at the oxide-rich Pd<sub>0.8</sub>W<sub>0.2</sub>/C shifted toward a higher potential. Which is consistent with the prediction of the high activity of Pd<sub>3</sub>W [47]. As mentioned above, the Pd<sub>0.8</sub>W<sub>0.2</sub> nanoparticles exhibit the smallest size and the largest EASA, which is a benefit for their electrocatalytic performance of ORR.

Chronoamperometry (CA) curves are often used to evaluate the stability of electrocatalysts [67,68]. Electrocatalytic stability of Pd/C and oxide-rich Pd<sub>0.8</sub>W<sub>0.2</sub>C catalysts were characterized by CA at 0.57 V vs. RHE in 0.1 M NaOH solution (Figure 7). At the beginning the CA current decreased rapidly, then the current density of each catalyst became relatively stable. The rapid decrease in the initial 1 or 2 s may be the charging current at the working electrode (WE). At the beginning of the CA measurements, the potential at the WE rapidly shifted to the set potential (0.57 V vs. RHE). The rapid shift of potential caused a charging current at the WE. Although the oxide-rich Pd<sub>0.8</sub>W<sub>0.2</sub>/C catalyst exhibits higher electrocatalytic stability than Pd/C, it is still difficult to draw a conclusion of whether the composition of the catalyst is unchanged during the ORR measurements. Catalysts with constant compositions such as pure Pd [69] or pure Pt [70] sometimes exhibit poor electrocatalytic stability. Therefore the high electrocatalytic stability does not mean constant composition. It can be seen from Figure 6 that Pd<sub>0.9</sub>W<sub>0.1</sub>/C also exhibits high activity. That means even if a half of the W/WO<sub>3</sub> de-alloyed from the Pd<sub>0.8</sub>W<sub>0.2</sub> nanoalloys, the Pd–W catalysts still maintain high activity. The current density ( $\text{mA}\cdot\text{mg Pd}^{-1}$ ) at the oxide-rich Pd<sub>0.8</sub>W<sub>0.2</sub>/C is more than 1.6 times of that at Pd/C.



**Figure 6.** Linear sweep voltammetry (LSV) of Pd/C (a), oxide-rich Pd<sub>0.6</sub>W<sub>0.4</sub>/C (b), oxide-rich Pd<sub>0.7</sub>W<sub>0.3</sub>/C (c), oxide-rich Pd<sub>0.8</sub>W<sub>0.2</sub>/C (d), oxide-rich Pd<sub>0.9</sub>W<sub>0.1</sub>/C (e) in 0.1 M NaOH solution saturated with O<sub>2</sub>. Rotating speed 2000 r/min. Scan rate 1 mV·s<sup>-1</sup>.



**Figure 7.** Electrochemical stability of Pd/C (a) and oxide-rich Pd<sub>0.8</sub>W<sub>0.2</sub>/C (b) in 0.1 mol/L NaOH solution saturated with O<sub>2</sub>. Potential 0.57 V vs. RHE. Rotating speed 2000 r/min.

Figure 8 shows the electrochemical impedance spectroscopy (EIS) of Pd/C and oxide-rich Pd<sub>0.8</sub>W<sub>0.2</sub>/C catalysts. EIS measurements were performed from 1 Hz to 100 kHz with 5 mV signals. The semicircle arc radius in the high-frequency region represents the charge transfer resistance (RCT). It can be seen that the charge transfer resistance of the oxide-rich Pd<sub>0.8</sub>W<sub>0.2</sub>/C is similar to that of Pd/C.

Figure 9 shows the Koutecky–Levich plots of oxide-rich Pd<sub>0.8</sub>W<sub>0.2</sub>/C catalyst, the transferred electron numbers of O<sub>2</sub> in ORR were determined by the Koutecky–Levich equation:

$$B = 0.2 nF (D_{O_2})^{2/3} \nu^{-1/6} C_{O_2}$$

where  $B$  is the reciprocal of the slope of the Koutecky–Levich plots,  $n$  is the number of electrons transferred,  $F$  is the Faraday constant,  $D$  is the diffusion coefficient of  $O_2$  in 0.1 M NaOH,  $\nu$  is the viscosity of the electrolyte, and  $C$  is the saturated concentration of  $O_2$  in 0.1 M NaOH [71]. Based on the Koutecky–Levich plots and the Koutecky–Levich equation, the calculated number of electrons transferred is 3.8. Thus there is mainly a 4-electron mechanism for the ORR at the oxide-rich  $Pd_{0.8}W_{0.2}/C$  catalyst.

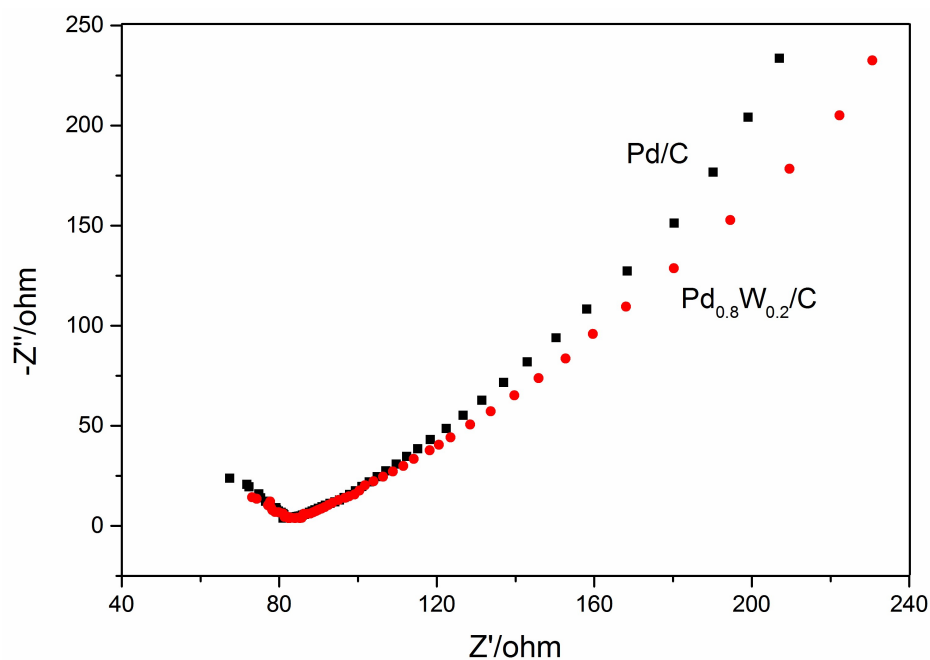


Figure 8. EIS of Pd/C and oxide-rich  $Pd_{0.8}W_{0.2}/C$  catalysts.

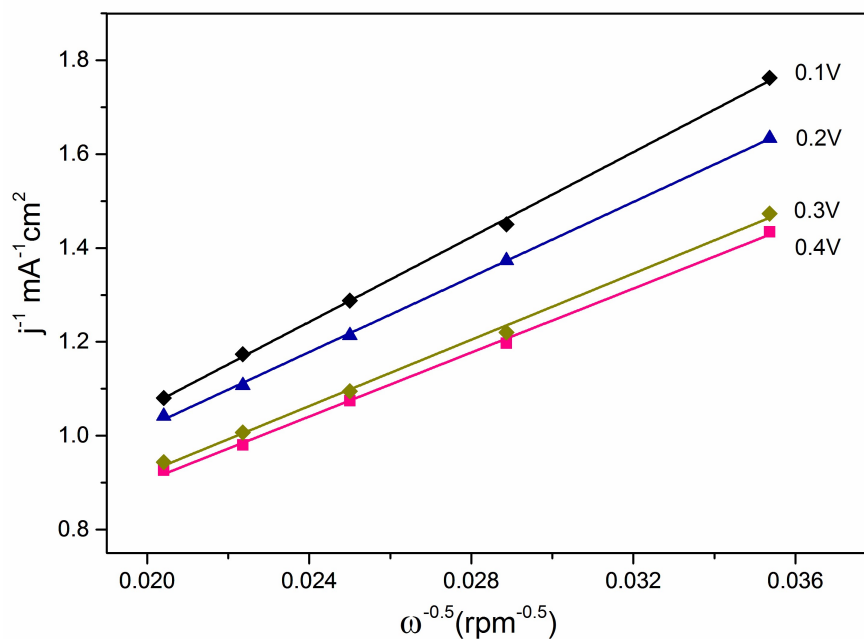


Figure 9. Koutecky–Levich plots of oxide-rich  $Pd_{0.8}W_{0.2}/C$  catalyst.

### 3. Materials and Methods

#### 3.1. Preparation and Characterization of the Catalysts

$\text{PdCl}_2$  was purchased from Sinopharm Chemical Reagent Co., Ltd. (Shanghai, China). The Vulcan carbon powder XC-72R was obtained from Cabot Corporation (Cabot Corp., Billerica, MA, USA). Nafion solution (5%) was obtained from DuPont (Delaware, DE, USA). All other chemicals were of analytical grade and used as acquired. Triple-distilled water was used through-out. The  $\text{WO}_3$  containing Pd–W catalysts were prepared with the reduction–oxidation procedures, schematically illustrated in Scheme 1.

Pd/C and PdW/C catalysts with a metal loading of 20 wt% were prepared by the  $\text{NaBH}_4$  chemical reduction method (Scheme 1, step 1) that we used before [72].  $\text{PdCl}_2$  and  $\text{Na}_2\text{WO}_4$  were used as the precursors. Electrocatalysts with different atomic ratios were controlled by the molar ratio of metal precursors. The Pd–W nanoalloys are easily oxidized in ambient air and formed the  $\text{WO}_3$ -contained Pd–W/C catalysts (Scheme 1, step 2).

The XRD was carried out by a Bruker D8 advance X-ray diffractometer (BRUKER AXS GMBH, Karlsruhe, Germany) operating at 40 keV and 30 mA with Cu  $\text{K}\alpha$  radiation source,  $\lambda = 0.15406$  nm. The TEM/HRTEM images were obtained on a JEOL JEM-2100 transmission electron microscope (JEOL, Tokyo, Japan). The content of metal elements on the surface of the samples was analyzed by EDS. The presence of the metal was excited by X-ray photoelectron spectroscopy (XPS) using Al  $\text{K}\alpha$  X-ray radiation on an ESCALAB 250 (Thermo Fisher SCIENTIFIC, Waltham, MA, USA) spectrometer. Peak fitting using Gaussian/Lorentzian (20% Gaussian) method after background subtraction using Shirley's method [73].

#### 3.2. Electrochemical Measurements

The electrochemical measurements were performed with CHI832B and CHI660E electrochemical workstations (CHI Instruments, Austin, TX, USA) and a conventional three-electrode electrochemical cell. A carbon-rod was used as the auxiliary electrode. A Hg/HgO electrode was used as the reference electrode. The working electrode was prepared by the following procedure: The glassy carbon electrode (GCE, 3 mm in diameter, LANLIKE, Tianjin, China) was carefully polished with 0.05  $\mu\text{m}$  alumina ( $\text{Al}_2\text{O}_3$ ) powder, and washed with triple-distilled water before use. Ten mg of the catalyst powder in a mixture of 0.5 mL water and 0.5 mL ethanol was ultrasonicated for 15 min to prepare the ink for catalysts. Twenty  $\mu\text{L}$  ( $2 \mu\text{L} \times 10$  times) of the ink was dropped on the GCE. Three  $\mu\text{L}$  of Nafion solution (5 wt.%) was dropped on the surface after the ink was dried in air.

### 4. Conclusions

The  $\text{WO}_3$  containing oxide-rich Pd–W/C catalysts were successful fabricated by reduction–oxidation procedures. The as prepared oxide-rich  $\text{Pd}_{0.8}\text{W}_{0.2}/\text{C}$  catalysts exhibit high electrocatalytic activity and stability. This demonstrates that the as prepared oxide-rich  $\text{Pd}_{0.8}\text{W}_{0.2}/\text{C}$  is a prospective candidate for the cathode of fuel cells operating with alkaline electrolyte.

**Author Contributions:** The corresponding author W.L. is the director of the other authors. W.L. and N.C. designed the experiments. N.C. and Z.G. carried out the experiments; X.X. and H.Z. analyzed the experimental results.

**Acknowledgments:** This work was supported by the Natural Science Foundation of Shandong Province (ZR2016BM31). We are greatly appreciate the contributions of Guang Dong, Xin Han, Haoquan Zhang, Shuzheng Xu, Peipei Yu and Mingchen Qin for their kindly repeated the experiments to make sure the data is repeatable, and proofreading the spellings.

**Conflicts of Interest:** The authors declare no conflict of interest.

## References

1. Lee, J.; Jeong, B.; Ocon, J.D. Oxygen electrocatalysis in chemical energy conversion and storage technologies. *Curr. Appl. Phys.* **2013**, *13*, 309–321. [[CrossRef](#)]
2. Shin, D.; Jeong, B.; Choun, M.; Ocon, J.D.; Lee, J. Diagnosis of the measurement inconsistencies of carbon-based electrocatalysts for the oxygen reduction reaction in alkaline media. *RSC Adv.* **2015**, *5*, 1571–1580. [[CrossRef](#)]
3. Wang, Y.-J.; Fang, N.Z.B.; Li, H.; Bi, X.T.; Wang, H. Carbon-Supported Pt-Based Alloy Electrocatalysts for the Oxygen Reduction Reaction in Polymer Electrolyte Membrane Fuel Cells: Particle Size, Shape, and Composition Manipulation and Their Impact to Activity. *Chem. Rev.* **2015**, *115*, 3433–3467. [[CrossRef](#)] [[PubMed](#)]
4. Tian, X.L.; Xu, Y.Y.; Zhang, W.; Wu, T.; Xia, B.Y.; Wang, X. Unsupported Platinum-Based Electrocatalysts for Oxygen Reduction Reaction. *ACS Energy Lett.* **2017**, *2*, 2035–2043. [[CrossRef](#)]
5. Wu, W.; Tang, Z.; Wang, K.; Liu, Z.; Li, L.; Chen, S. Peptide templated AuPt alloyed nanoparticles as highly efficient bi-functional electrocatalysts for both oxygen reduction reaction and hydrogen evolution reaction. *Electrochim. Acta* **2018**, *260*, 168–176. [[CrossRef](#)]
6. Zhang, L.; Chang, Q.; Chen, H.; Shao, M. Recent advances in palladium-based electrocatalysts for fuel cell reactions and hydrogen evolution reaction. *Nano Energy* **2016**, *29*, 198–219. [[CrossRef](#)]
7. Kühn, S.; Strasser, P. Oxygen Electrocatalysis on Dealloyed Pt Nanocatalysts. *Top. Catal.* **2016**, *59*, 1628–1637. [[CrossRef](#)]
8. Du, C.; Gao, X.; Chen, W. Recent developments in copper-based, non-noble metal electrocatalysts for the oxygen reduction reaction. *Chin. J. Catal.* **2016**, *37*, 1049–1061. [[CrossRef](#)]
9. Vij, V.; Sultan, S.; Harzandi, A.M.; Meena, A.; Tiwari, J.N.; Lee, W.; Yoon, T.; Kim, K.S. Nickel-Based Electrocatalysts for Energy-Related Applications: Oxygen Reduction, Oxygen Evolution, and Hydrogen Evolution Reactions. *ACS Catal.* **2017**, *7*, 7196–7225. [[CrossRef](#)]
10. Yang, L.; Zhao, Y.; Chen, S.; Wu, Q.; Wang, X.; Hu, Z. A mini review on carbon-based metal-free electrocatalysts for oxygen reduction reaction. *Chin. J. Catal.* **2013**, *34*, 1986–1991. [[CrossRef](#)]
11. Wu, G.; Santandreu, A.; Kellogg, W.; Gupta, S.; Ogoke, O.; Zhang, H.; Wang, H.-L.; Dai, L. Carbon nanocomposite catalysts for oxygen reduction and evolution reactions: From nitrogen doping to transition-metal addition. *Nano Energy* **2016**, *29*, 83–110. [[CrossRef](#)]
12. Shahgaldi, S.; Hamelin, J. Improved carbon nanostructures as a novel catalyst support in the cathode side of PEMFC: A critical review. *Carbon* **2015**, *94*, 705–728. [[CrossRef](#)]
13. Bezerra, C.W.B.; Zhang, L.; Lee, K.; Liu, H.; Marques, A.L.B.; Marques, E.P.; Wang, H.; Zhang, J. A review of Fe-N/C and Co-N/C catalysts for the oxygen reduction reaction. *Electrochim. Acta* **2008**, *53*, 4937–4951. [[CrossRef](#)]
14. Osgood, H.; Devaguptapu, S.V.; Xu, H.; Cho, J.; Wu, G. Transition metal (Fe, Co, Ni, and Mn) oxides for oxygen reduction and evolution bifunctional catalysts in alkaline media. *Nano Today* **2016**, *11*, 601–625. [[CrossRef](#)]
15. Stoerzinger, K.A.; Risch, M.; Han, B.; Shao-Horn, Y. Recent Insights into Manganese Oxides in Catalyzing Oxygen Reduction Kinetics. *ACS Catal.* **2015**, *5*, 6021–6031. [[CrossRef](#)]
16. Fu, S.; Zhu, C.; Song, J.; Du, D.; Lin, Y. Metal-Organic Framework-Derived Non-Precious Metal Nanocatalysts for Oxygen Reduction Reaction. *Adv. Energy Mater.* **2017**, *7*, 1700363. [[CrossRef](#)]
17. Song, Z.; Cheng, N.; Lushington, A.; Sun, X. Recent Progress on MOF-Derived Nanomaterials as Advanced Electrocatalysts in Fuel Cells. *Catalysts* **2016**, *6*, 116. [[CrossRef](#)]
18. Choi, J.Y.; Higgins, D.; Jiang, G.; Hsu, R.; Qiao, J.; Chen, Z. Iron-tetracyanobenzene complex derived non-precious catalyst for oxygen reduction reaction. *Electrochim. Acta* **2015**, *162*, 224–229. [[CrossRef](#)]
19. Thorseth, M.A.; Tornow, C.E.; Tse, E.C.M.; Gewirth, A.A. Cu complexes that catalyze the oxygen reduction reaction. *Coord. Chem. Rev.* **2013**, *257*, 130–139. [[CrossRef](#)]
20. Fernández, J.L.; Mano, N.; Heller, A.; Bard, A.J. Optimization of “Wired” Enzyme O<sub>2</sub>-Electroreduction Catalyst compositions by Scanning Electrochemical Microscopy. *Angew. Chem. Int. Ed.* **2004**, *43*, 6355–6357. [[CrossRef](#)] [[PubMed](#)]
21. Mano, N.; Fernández, J.L.; Kim, Y.; Shin, W.; Bard, A.J.; Heller, A. Oxygen is Electroreduced to Water on a “Wired” Enzyme Electrode at a Lesser Overpotential than on Platinum. *J. Am. Chem. Soc.* **2003**, *125*, 15290–15291. [[CrossRef](#)] [[PubMed](#)]

22. Chakraborty, S.; Babanova, S.; Rocha, R.C.; Desireddy, A.; Artyushkova, K.; Boncella, A.E.; Atanassov, P.; Martinez, J.S. A Hybrid DNA-Templated Gold Nanocluster for Enhanced Enzymatic Reduction of Oxygen. *J. Am. Chem. Soc.* **2015**, *137*, 11678–11687. [[CrossRef](#)] [[PubMed](#)]
23. Husband, J.; Aaron, M.S.; Bains, R.K.; Lewis, A.R.; Warren, J.J. Catalytic reduction of dioxygen with modified *Thermus thermophilus* cytochrome c552. *J. Inorg. Biochem.* **2016**, *157*, 8–14. [[CrossRef](#)] [[PubMed](#)]
24. Tsujimura, S.; Suraniti, E.; Durand, F.; Mano, N. Oxygen reduction reactions of the thermostable bilirubin oxidase from *Bacillus pumilus* on mesoporous carbon-cryogel electrodes. *Electrochim. Acta* **2014**, *117*, 263–267. [[CrossRef](#)]
25. Hu, Y.; Jensen, J.O.; Zhang, W.; Cleemann, L.N.; Xing, W.; Bjerrum, N.J.; Li, Q. Hollow spheres of iron carbide nanoparticles encased in graphitic layers as oxygen reduction catalysts. *Angew. Chem. Int. Ed.* **2014**, *53*, 3675–3679. [[CrossRef](#)] [[PubMed](#)]
26. Wang, W.; Xue, S.; Li, J.; Wang, F.; Kang, Y.; Lei, Z. Cerium carbide embedded in nitrogen-doped carbon as a highly active electrocatalyst for oxygen reduction reaction. *J. Power Sources* **2017**, *359*, 487–493. [[CrossRef](#)]
27. Guoa, J.; Maob, Z.; Yana, X.; Suc, R.; Guanc, P.; Xua, B.; Zhangb, X.; Qinb, G.; Pennycookd, S.J. Ultrasmall tungsten carbide catalysts stabilized in graphitic layers for high-performance oxygen reduction reaction. *Nano Energy* **2016**, *28*, 261–268. [[CrossRef](#)]
28. Bukola, S.; Merzougui, B.; Akinpelu, A.; Zeama, M. Cobalt and Nitrogen Co-Doped Tungsten Carbide Catalyst for Oxygen Reduction and Hydrogen Evolution Reactions. *Electrochim. Acta* **2016**, *190*, 1113–1123. [[CrossRef](#)]
29. Stacy, J.; Regmi, Y.N.; Leonard, B.; Fan, M. The recent progress and future of oxygen reduction reaction catalysis: A review. *Renew. Sustain. Energy Rev.* **2017**, *69*, 401–414. [[CrossRef](#)]
30. Erikson, H.; Sarapuu, A.; Solla-Gullón, J.; Tammeveski, K.J. Recent progress in oxygen reduction electrocatalysis on Pd-based catalysts. *Electroanal. Chem.* **2016**, *780*, 327–336. [[CrossRef](#)]
31. Antolini, E. Palladium in fuel cell catalysis. *Energy Environ. Sci.* **2009**, *2*, 915–931. [[CrossRef](#)]
32. Nie, Y.; Li, L.; Wei, Z. Recent advancements in Pt and Pt-free catalysts for oxygen reduction reaction. *Chem. Soc. Rev.* **2015**, *44*, 2168–2201. [[CrossRef](#)] [[PubMed](#)]
33. Higgins, D.; Zamani, P.; Yu, A.; Chen, Z. The application of graphene and its composites in oxygen reduction electrocatalysis: A perspective and review of recent progress. *Energy Environ. Sci.* **2016**, *9*, 357–390. [[CrossRef](#)]
34. Ge, X.; Sumboja, A.; Wu, D.; An, T.; Li, B.; Goh, F.W.T.; Hor, T.S.A.; Zong, Y.; Liu, Z. Oxygen Reduction in Alkaline Media: From Mechanisms to Recent Advances of Catalysts. *ACS Catal.* **2015**, *5*, 4643–4667. [[CrossRef](#)]
35. Lide, D.R. (Ed.) *CRC Handbook of Chemistry and Physics*; CRC Press (Taylor and Francis Group): Boca Raton, FL, USA, 2009; Section 8, p. 23.
36. Li, B.; Prakash, J. Oxygen reduction reaction on carbon supported Palladium–Nickel alloys in alkaline media. *Electrochem. Commun.* **2009**, *11*, 1162–1165. [[CrossRef](#)]
37. Alexeyeva, N.; Sarapuu, A.; Tammeveski, K.; Vidal-Iglesias, F.J.; Solla-Gullón, J.; Feliu, J.M. Electroreduction of oxygen on Vulcan carbon supported Pd nanoparticles and Pd–M nanoalloys in acid and alkaline solutions. *Electrochim. Acta* **2011**, *56*, 6702–6708. [[CrossRef](#)]
38. Arenz, M.; Schmidt, T.J.; Wandelt, K.; Ross, P.N.; Markovic, N.M. The Oxygen Reduction Reaction on Thin Palladium Films Supported on a Pt(111) Electrode. *J. Phys. Chem. B* **2003**, *107*, 9813–9819. [[CrossRef](#)]
39. Li, Y.; Lin, S.; Ren, X.; Mi, H.; Zhang, P.; Sun, L.; Deng, L.; Gao, Y. One-step rapid in-situ synthesis of nitrogen and sulfur co-doped three-dimensional honeycomb-ordered carbon supported PdNi nanoparticles as efficient electrocatalyst for oxygen reduction reaction in alkaline solution. *Electrochim. Acta* **2017**, *253*, 445–454. [[CrossRef](#)]
40. Li, J.; Zhou, H.; Zhuo, H.; Wei, Z.; Zhuang, G.; Zhong, X.; Deng, S.; Li, X.; Wang, J. Oxygen vacancies on TiO<sub>2</sub> promoted the activity and stability of supported Pd nanoparticles for the oxygen reduction reaction. *J. Mater. Chem. A* **2018**, *6*, 2264–2272. [[CrossRef](#)]
41. Li, Y.; Li, W.; Ke, T.; Zhang, P.; Ren, X.; Deng, L. Microwave-assisted synthesis of sulfur-doped graphene supported PdW nanoparticles as a high performance electrocatalyst for the oxygen reduction reaction. *Electrochem. Commun.* **2016**, *69*, 68–71. [[CrossRef](#)]
42. Sun, L.; Liao, B.; Ren, X.; Li, Y.; Zhang, P.; Deng, L.; Gao, Y. Ternary PdNi-based nanocrystals supported on nitrogen-doped reduced graphene oxide as highly active electrocatalysts for the oxygen reduction reaction. *Electrochim. Acta* **2017**, *235*, 543–552. [[CrossRef](#)]

43. Ren, X.; Liao, B.; Li, Y.; Zhang, P.; Deng, L.; Gao, Y. Facile synthesis of PdSnCo/nitrogen-doped reduced graphene as a highly active catalyst for lithium-air batteries. *Electrochimica Acta* **2017**, *228*, 36–44. [[CrossRef](#)]
44. Yasmin, S.; Cho, S.; Jeon, S. Electrochemically reduced graphene-oxide supported bimetallic nanoparticles highly efficient for oxygen reduction reaction with excellent methanol tolerance. *Appl. Surf. Sci.* **2018**, *434*, 905–912. [[CrossRef](#)]
45. Xue, Q.; Xu, G.; Mao, R.; Liu, H.; Zeng, J.; Jiang, J.; Chen, Y. Polyethyleneimine modified AuPd@PdAu alloy nanocrystals as advanced electrocatalysts towards the oxygen reduction reaction. *J. Energy Chem.* **2017**, *26*, 1153–1159. [[CrossRef](#)]
46. Kabir, S.; Serov, A.; Artyushkova, K.; Atanassov, P. Nitrogen-Doped Three-Dimensional Graphene-Supported Palladium Nanocomposites: High-Performance Cathode Catalysts for Oxygen Reduction Reactions. *ACS Catal.* **2017**, *7*, 6609–6618. [[CrossRef](#)]
47. Yu, T.H.; Sha, Y.; Merinov, B.V.; Goddard, W.A. Improved Non-Pt Alloys for the Oxygen Reduction Reaction at Fuel Cell Cathodes Predicted from Quantum Mechanics. *J. Phys. Chem. C* **2010**, *114*, 11527–11533. [[CrossRef](#)]
48. Li, W.; Fan, F.-F.; Bard, A.J. The application of scanning electrochemical microscopy to the discovery of Pd–W electrocatalysts for the oxygen reduction reaction that demonstrate high activity, stability, and methanol tolerance. *J. Solid State Electrochem.* **2012**, *16*, 2563–2568. [[CrossRef](#)]
49. Luo, Z.; Martí-Sánchez, S.; Nafria, R.; Joshua, G.S.; de la Mata, M.; Guardia, P.; Flox, C.; Martínez-Boubeta, C.; Simeonidis, K.; Llorca, J.; et al. Fe<sub>3</sub>O<sub>4</sub>@NiFeO<sub>x</sub> nanoparticles with enhanced electrocatalytic properties for oxygen evolution in carbonate electrolyte. *ACS Appl. Mater. Interfaces* **2016**, *8*, 29461–29469. [[CrossRef](#)] [[PubMed](#)]
50. Tauster, S.J.; Fung, S.C.; Baker, R.T.K.; Horsley, J.A. Strong Interactions in Supported-Metal Catalysts. *Science* **1981**, *211*, 1121–1125. [[CrossRef](#)] [[PubMed](#)]
51. Ocal, C.; Ferrer, S. The strong metal support interaction (SMSI) in Pt-TiO<sub>2</sub> model catalysts, A new CO adsorption state on Pt-Ti atoms. *J. Chem. Phys.* **1986**, *84*, 6474–6478. [[CrossRef](#)]
52. Zhang, S.; Plessow, P.N.; Willis, J.J.; Dai, S.; Xu, M.; Graham, G.W.; Cargnello, M.; Abild-Pedersen, F.; Pan, X. Dynamical Observation and Detailed Description of Catalysts under Strong Metal–Support Interaction. *Nano Lett.* **2016**, *16*, 4528–4534. [[CrossRef](#)] [[PubMed](#)]
53. Wang, L.; Zhang, J.; Zhu, Y.; Xu, S.; Wang, C.; Bian, C.; Meng, X.; Xiao, F.-S. Strong Metal–Support Interactions Achieved by Hydroxide-to-Oxide Support Transformation for Preparation of Sinter-Resistant Gold Nanoparticle Catalysts. *ACS Catal.* **2017**, *7*, 7461–7465. [[CrossRef](#)]
54. Jia, Q.; Ghoshal, S.; Li, J.; Liang, W.; Meng, G.; Che, H.; Zhang, S.; Ma, Z.; Mukerjee, S. Metal and Metal Oxide Interactions and Their Catalytic Consequences for Oxygen Reduction Reaction. *J. Am. Chem. Soc.* **2017**, *139*, 7893–7903. [[CrossRef](#)] [[PubMed](#)]
55. Liu, T.; Guo, Z.; Li, W.; Pang, Z.; Tong, Q. Oxidation of Ethanol on Carbon-Supported Oxide-Rich Pd–W Bimetallic Nanoparticles in Alkaline Media. *Russ. J. Phys. Chem. A* **2017**, *91*, 1994–2001. [[CrossRef](#)]
56. Guo, Z.; Liu, T.; Li, W.; Zhang, C.; Zhang, D.; Pang, Z. Carbon Supported Oxide-Rich Pd–Cu Bimetallic Electrocatalysts for Ethanol Electrooxidation in Alkaline Media Enhanced by Cu/CuOx. *Catalysts* **2016**, *6*, 62. [[CrossRef](#)]
57. Staikov, G. Monte Carlo method. In *Electrocrystallization in Nanotechnology*; Wiley-VCH: Weinheim, Germany, 2007; Chapter 2.3.
58. Kolb, D.M.; Engelmann, G.E.; Ziegler, J.C. On the unusual electrochemical stability of nanofabricated copper clusters. *Angew. Chem. Int. Ed.* **2010**, *39*, 1123–1125. [[CrossRef](#)]
59. Lv, M.; Li, W.; Liu, H.; Wen, W.; Dong, G.; Liu, J.; Peng, K. Enhancement of the formic acid electrooxidation activity of palladium using graphene/carbon black binary carbon supports. *Chin. J. Catal.* **2017**, *38*, 939–947. [[CrossRef](#)]
60. Nutor, R.K.; Xu, X.; Fan, X.; Ren, S.; He, X.; Fang, Y. Structural anisotropy in FeCuNbSiB alloys: An in situ synchrotron XRD study. *J. Magn. Magn. Mater.* **2018**, *454*, 51–56. [[CrossRef](#)]
61. Ohnuma, M.; Hono, K. Origin of the magnetic anisotropy induced by stress annealing in Fe-based nanocrystalline alloy. *Appl. Phys. Lett.* **2005**, *86*, 152513. [[CrossRef](#)]
62. Holzwarth, U.; Gibson, N. The Scherrer equation versus the ‘Debye–Scherrer equation’. *Nat. Nanotechnol.* **2011**, *6*, 534. [[CrossRef](#)] [[PubMed](#)]

63. Yu, B.; Wen, W.; Li, W.; Yang, Y.; Hou, D.; Liu, C. Fabrication of high performance carbon-supported ternary Pd-Cu-Fe electrocatalysts for formic acid electrooxidation via partly galvanic sacrifice of tunable binary Cu-Fe alloy templates. *Electrochim. Acta* **2016**, *196*, 223–230. [[CrossRef](#)]
64. Wu, Q.; Rao, Z.; Yuan, L.; Jiang, L.; Sun, G.; Ruan, J.; Zhou, Z.; Sang, S. Carbon supported PdO with improved activity and stability for oxygen reduction reaction in alkaline solution. *Electrochim. Acta* **2014**, *150*, 157–166. [[CrossRef](#)]
65. Ji, X.; Ma, M.; Ge, R.; Ren, X.; Wang, H.; Liu, J.; Liu, Z.; Asiri, A.M.; Sun, X. WO<sub>3</sub> Nanoarray: An Efficient Electrochemical Oxygen Evolution Catalyst Electrode Operating in Alkaline Solution. *Inorg. Chem.* **2017**, *56*, 14743–14746. [[CrossRef](#)] [[PubMed](#)]
66. Zhang, Z.; Wang, X.; Cui, Z.; Liu, C.; Lu, T.; Xing, W. Pd nanoparticles supported on WO<sub>3</sub>/C hybrid material as catalyst for oxygen reduction reaction. *J. Power Sources* **2008**, *185*, 941–945. [[CrossRef](#)]
67. Foruzin, L.J.; Rezvani, Z.; Shishavan, Y.H. Biuck Habibi Ni<sub>2</sub>Zn<sub>0.5</sub>Fe-LDH modified carbon paste electrode as an efficient electrocatalyst for water oxidation in neutral media. *Int. J. Hydrog. Energy* **2018**, *43*, 150–160. [[CrossRef](#)]
68. Habibi, B.; Ghaderi, S. Synthesis, characterization and electrocatalytic activity of Co@Pt nanoparticles supported on carbon-ceramic substrate for fuel cell applications. *Int. J. Hydrog. Energy* **2015**, *40*, 5115–5125. [[CrossRef](#)]
69. Jung, W.; Han, J.; Ha, S. Analysis of palladium-based anode electrode using electrochemical impedance spectra in direct formic acid fuel cells. *J. Power Sources* **2007**, *173*, 53–59. [[CrossRef](#)]
70. Ferreira, P.J.; la O', G.J.; Shao-Horn, Y. Instability of Pt/C electrocatalysts in proton exchange membrane fuel cells. *J. Electrochem. Soc.* **2005**, *152*, A2256–A2271. [[CrossRef](#)]
71. Hosseini, M.G.; Zardari, P. Electrocatalysis of oxygen reduction on multi-walled carbon nanotube supported Ru-based catalysts in alkaline media. *Int. J. Hydrog. Energy* **2016**, *41*, 8803–8818. [[CrossRef](#)]
72. Wen, W.J.; Li, C.Y.; Li, W.P.; Tian, Y. Carbon-supported Pd-Cr electrocatalysts for the electrooxidation of formic acid that demonstrate high activity and stability. *Electrochim. Acta* **2013**, *109*, 201–206. [[CrossRef](#)]
73. Shirley, D.A. High-resolution X-ray photoemission spectrum of the valence bands of gold. *Phys. Rev. B* **1972**, *5*, 4709. [[CrossRef](#)]



© 2018 by the authors. Licensee MDPI, Basel, Switzerland. This article is an open access article distributed under the terms and conditions of the Creative Commons Attribution (CC BY) license (<http://creativecommons.org/licenses/by/4.0/>).